communications materials

Article

A Nature Portfolio journal

https://doi.org/10.1038/s43246-026-01342-3

Non-equilibrium stabilization of a ductile disordered phase in a high-aluminum refractory alloy

Check for updates

Jin Wang [1] ✉, Nicolas J. Peter [1], Liuliu Han [2,3], Alisson Kwiatkowski da Silva [2], Fiona Schulz[4], Eric A. Jägle [4] & Ruth Schwaiger [1,5] ✉

High-aluminum refractory compositionally complex alloys are intrinsically brittle due to ordering and grain-boundary intermetallics. We show that extreme thermal gradients during selective laser melting kinetically suppress these transformations in NbMoCrTiAl, stabilizing a disordered A2 solid solution despite strong thermodynamic driving forces for B2 ordering and C14/A15 formation. Multi-scale characterization and kinetic simulations reveal how rapid liquid-solid and solid-state transformations dissolve intermetallic phases and prevent reordering during cooling. The resulting precipitate-free A2 microstructure exhibits substantially enhanced room-temperature plasticity, overcoming brittleness without compositional modification. Our results establish non-equilibrium processing as a route to access otherwise inaccessible phase states in refractory complex alloys, expanding the design space of high-temperature structural materials.

High-aluminum refractory compositionally complex alloys (RCCAs) combine reduced density with high melting temperatures and promising oxidation resistance, making them attractive candidates for next-generation high-temperature structural applications[1–5]. However, their room-temperature brittleness severely limits practical use. In alloys such as NbMoCrTiAl, strong negative mixing enthalpies between aluminum and refractory elements promote long-range ordering and the formation of intermetallic phases, including B2 matrices and grain-boundary C14 and A15 compounds[6–8]. These ordered and segregated microstructures restrict dislocation mobility[9], and facilitate intergranular fracture[8], rendering the alloys intrinsically brittle.

Attempts to mitigate this brittleness typically rely on reducing aluminum content to suppress ordering in matrices and intermetallic formation[10–16]. While effective in improving ductility, this approach compromises density reduction and oxidation resistance, reintroducing the very trade-offs RCCAs seek to overcome. A fundamental question, therefore, emerges: can the accessible phase space of high-Al RCCAs be expanded without altering composition?

Equilibrium thermodynamics predicts that NbMoCrTiAl forms a disordered A2 solid solution only at elevated temperatures, decomposing upon cooling into ordered B2 and intermetallic phases[7]. Under conventional processing conditions, cooling rates are insufficient to suppress these transformations. Yet phase stability in complex alloys is governed not only by thermodynamics but also by kinetic constraints[17]. If transformations such as ordering and precipitation can be kinetically bypassed, metastable disordered states may be retained at room temperature, potentially restoring ductility while preserving composition.

Here, we demonstrate that extreme thermal gradients[17–19] during selective laser melting provide access to such kinetically stabilized phase states. Using NbMoCrTiAl as a model high-Al RCCA, we show that ultrafast heating and cooling suppress long-range ordering and dissolve grain-boundary intermetallics, stabilizing a disordered A2 solid solution across both molten and heat-affected regions. Correlative multi-scale characterization combined with thermodynamic and kinetic simulations reveals how rapid liquid–solid and solid-state transformations compete with diffusion and ordering kinetics to prevent reprecipitation during cooling. The resulting precipitate-free A2 microstructure exhibits markedly enhanced room-temperature plasticity in micromechanical tests.

These findings establish non-equilibrium thermal processing as a route to access otherwise thermodynamically inaccessible phase states in refractory complex alloys, expanding the design space of high-temperature structural materials through kinetic control[20].

[1]Institute of Energy Materials and Devices -IMD-1: Structure and Function of Materials, Forschungszentrum Juelich GmbH, Juelich, Germany. [2]Max Planck Institute for Sustainable Materials, Düsseldorf, Germany. [3]Suzhou National Laboratory, Suzhou, China. [4]Universität der Bundeswehr München, Institute of Materials Science, Neubiberg, Germany. [5]Chair of Energy Engineering Materials, Faculty 5, RWTH Aachen University, Aachen, Germany. ✉e-mail: jin.wang@fz-juelich.de; r.schwaiger@fz-juelich.de

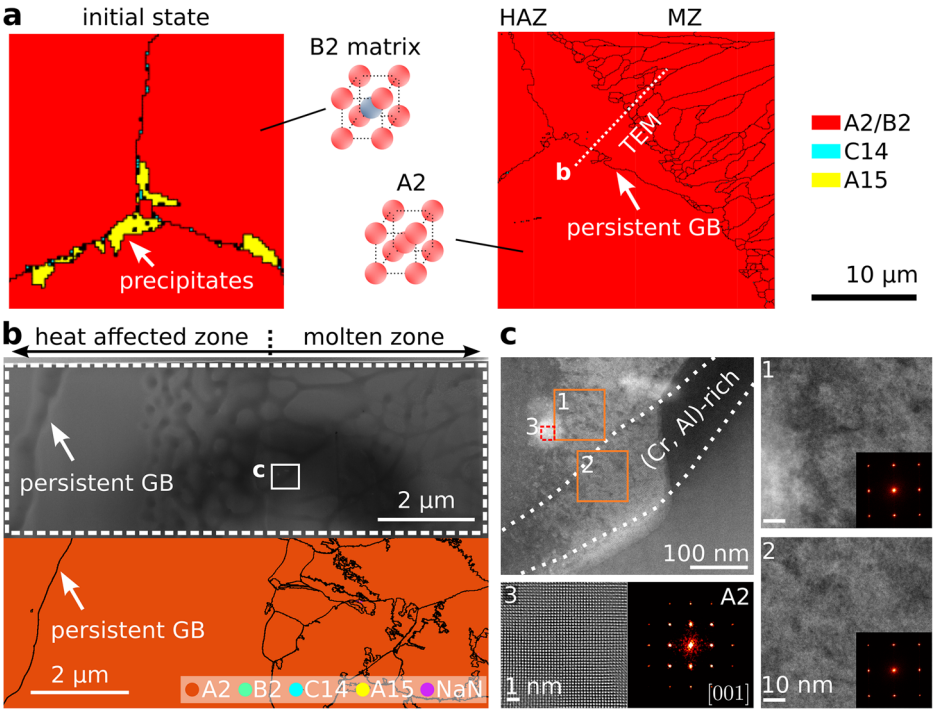

Fig. 1 | Kinetic suppression of ordering and intermetallic phases under extreme thermal gradients. a EBSD phase maps comparing the initial homogenized NbMoCrTiAl alloy, showing an ordered B2 matrix decorated by C14 and A15 intermetallic phases along grain boundaries, with the alloy after selective laser melting, revealing complete disappearance of grain-boundary intermetallics within the molten zone (MZ) and heat-affected zone (HAZ). **b** STEM image and 4D-STEM phase map from the laser-affected region showing a homogeneous matrix without secondary phases. **c** STEM diffraction patterns confirming stabilization of a disordered A2 structure in both regions of different chemical compositions within the laser-processed area. The sharp spatial transition between precipitate-containing and precipitate-free regions indicates that the imposed thermal cycle suppresses both intermetallic formation and long-range ordering despite the high aluminum content.

Results

Microstructure

The homogenized NbMoCrTiAl alloy exhibits the complex microstructure expected for high-Al refractory compositionally complex alloys. Electron backscatter diffraction (EBSD) phase maps (Fig. 1a) reveal a matrix dominated by an ordered B2 structure together with intermetallic precipitates decorating grain boundaries. Two types of intermetallic phases are observed: a C14 Laves phase (identified as Cr_2Nb) and an A15 phase (identified as $AlNb_3$), both preferentially located at grain boundaries and triple junctions.

Energy-dispersive X-ray spectroscopy confirms strong elemental partitioning associated with these phases, with Cr enrichment at grain boundaries and Nb–Al enrichment within the intermetallic compounds (Fig. S.3 in the Supplementary information). Atomic-resolution STEM further reveals that the intragranular matrix is an ordered B2 phase with CsCl-type atomic ordering[9].

This microstructure is consistent with previous reports on NbMoCrTiAl[7,8,21] and reflects the strong thermodynamic driving force for chemical ordering and intermetallic formation in Al-containing refractory alloys. The presence of grain-boundary precipitates together with long-range ordering in the matrix is known to severely restrict dislocation mobility and promote brittle fracture.

Selective laser melting dramatically alters this microstructure. EBSD phase maps acquired after single-track laser scanning reveal the complete disappearance of grain-boundary precipitates within both the molten zone (MZ) and the adjacent heat-affected zone (HAZ) (Fig. 1a). In contrast, precipitate-decorated grain boundaries remain visible in regions outside the laser-affected area (Fig. S.1d and e in the Supplementary information), indicating that the transformation is spatially confined to the thermal gradient imposed by the laser.

Grain refinement is also observed within the MZ, while coarse grains from the original microstructure persist in the HAZ. Importantly, even these persistent grain boundaries are free of C14, and A15 precipitates in the processed region. The sharp spatial transition between precipitate-containing and precipitate-free microstructures indicates that the imposed thermal cycle locally suppresses the formation of intermetallic phases despite the high aluminum content.

To determine whether laser processing also affects the ordering of the matrix, atomic-resolution STEM and 4D-STEM diffraction mapping were performed across the MZ-HAZ boundary (Fig. 1b). High-angle annular dark-field images reveal a homogeneous matrix structure extending from the MZ into the HAZ over a distance of ~2 µm.

Electron diffraction patterns obtained from both regions (Fig. 1c) exhibit reflections characteristic of a body-centered cubic lattice without superlattice peaks associated with B2 ordering. Corresponding phase maps derived from 4D-STEM confirm that the matrix in the entire analyzed region was identified as A2-type.

These observations demonstrate that laser processing not only dissolves intermetallic precipitates but also disorders the B2 matrix, stabilizing a disordered A2 structure at room temperature.

Although the matrix remains single-phase, nanoscale compositional heterogeneity is observed within the processed region. STEM-EDS maps reveal a maze-like contrast corresponding to alternating (Cr,Al)-rich and (Nb,Mo)-rich regions within both the MZ and the adjacent HAZ (Fig. 2a). Orientation mapping confirms that this contrast arises from chemical segregation rather than structural phase differences (Fig. 2a).

Atom probe tomography provides near-atomic-scale confirmation of this segregation (Fig. 2b–d). Three-dimensional reconstructions reveal compositional fluctuations corresponding to dendritic and interdendritic regions formed during rapid solidification. One-dimensional concentration profiles across these interfaces show enrichment of Cr and Al in interdendritic regions and enrichment of Nb and Mo in dendritic cores.

Despite this microsegregation, neither C14 nor A15 intermetallic phases are detected in the atom probe data or in electron diffraction. The observed segregation pattern is therefore consistent with microdendritic solidification occurring under conditions where nucleation and growth of equilibrium intermetallic phases are kinetically suppressed.

Non-equilibrium phase transformation

Thermodynamic calculations predict that the disordered A2 phase in NbMoCrTiAl is stable only at elevated temperatures and should transform to an ordered B2 structure accompanied by C14 and A15 intermetallic phases upon cooling (Fig. 3a, details in the Supplementary information-Thermodynamic and kinetic analysis). However, finite-element simulations

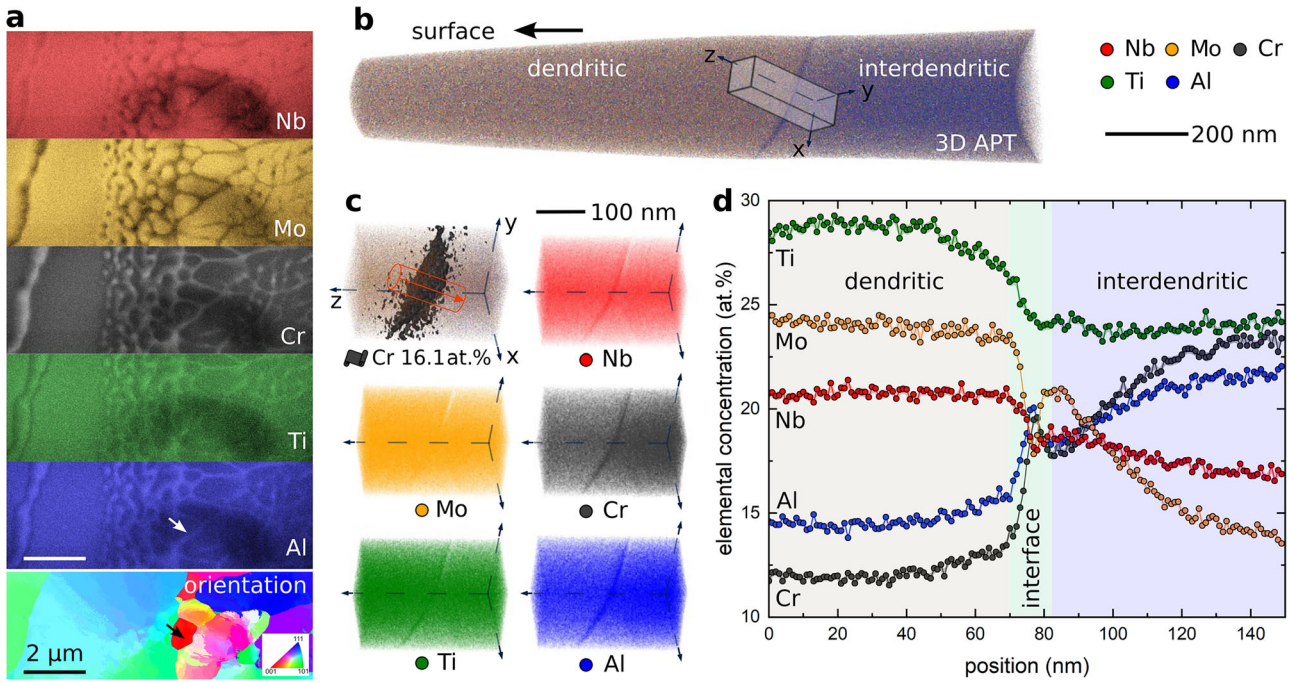

Fig. 2 | Rapid solidification produces microsegregation without intermetallic nucleation. a STEM-EDS elemental maps from the molten and heat-affected zones showing sub-micrometer segregation between refractory-rich and Al–Cr-rich regions following rapid solidification. A 4D-STEM orientation map illustrates the grains in the molten zone, showing the partial overlap of microsegregation and grain boundaries. The arrow marks the region shown in Fig. 1c. **b** Atom probe reconstruction from the same region, revealing compositional fluctuations at the nanoscale. **c** An enlarged view of a cuboidal region of interest showing the interface between segregated regions of higher Cr content and the corresponding individual elemental distributions. **d** One-dimensional concentration profiles across segregated regions, indicating partitioning consistent with dendritic solidification. Despite local compositional heterogeneity, no C14 or A15 intermetallic phases are detected, indicating that nucleation and growth are kinetically suppressed under the imposed cooling rates.

of the laser process reveal extremely rapid thermal cycles (Fig. S.8 in the Supplementary information).

Transient temperature profiles extracted from the simulations for the representative 150 W, 500 mm s^{-1} single-track condition (Fig. 3b) indicate heating and cooling rates on the order of 10^6 K s^{-1}, with local cooling rates of 6.4×10^5 to 1.4×10^6 K s^{-1} across the melt-pool boundary and adjacent heat-affected zone (see details in the Supplementary information-Thermodynamic and kinetic analysis). Material within approximately 50 µm of the melt pool center exceeds the liquidus temperature, while regions near the boundary are heated above the solidus but remain partially solid.

Diffusion simulations based on these thermal profiles show that rapid heating can dissolve existing intermetallic phases, while the subsequent quenching prevents their reprecipitation (Fig. 3c and d). Similarly, the residence time near the B2 ordering temperature range of 1220–1230 °C is too short for long-range diffusion required to restore chemical order (see Supplementary information-Thermodynamic and kinetic analysis). These simulated cooling rates are consistent with the experimentally observed phase state: 4D-STEM/diffraction patterns show no detectable long-range B2 superlattice reflections, EBSD phase mapping, and 4D-STEM diffraction analyses show no detectable C14/A15 precipitates within the analyzed laser-affected regions. As a result, both intermetallic formation and long-range ordering are kinetically bypassed during the thermal cycle.

Mechanical response of stabilized disordered phase

The microstructural transformation induced by laser processing has a pronounced effect on local mechanical behavior. High-resolution nanoindentation mapping (Fig. 4a) reveals a systematic reduction in hardness within the laser-affected region relative to the initial microstructure. Statistical analysis (Fig. 4b, details in the Supplementary information-Statistical analysis of nanoindentation data) of more than 6400 indents shows that the high-hardness population associated with intermetallic phases disappears after processing.

Microscale bending experiments (Fig. 4c and d, details in the Supplementary information-Analysis of bending experiments) further highlight the mechanical responses of the stabilized A2 phase. Cantilevers fabricated from the initial B2-containing microstructure exhibit brittle fracture shortly after yielding. In contrast, cantilevers extracted from the laser-affected region sustain significant post-yield plastic deformation before failure. Dense slip traces observed near the fixed end indicate active dislocation slip during deformation.

Engineering stress–strain curves derived from these experiments show comparable yield stresses for both microstructures but markedly enhanced post-yield bending deformation in the A2-stabilized region (Fig. 4d). The transition from an ordered, precipitate-decorated microstructure to a disordered, precipitate-free matrix therefore alleviates both grain-boundary crack initiation and restricted dislocation mobility.

Discussion

The microstructural transformation observed here demonstrates that phase stability in high-aluminum refractory compositionally complex alloys is not solely governed by equilibrium thermodynamics, but can be profoundly altered by kinetic constraints imposed during extreme thermal cycling. In NbMoCrTiAl, conventional processing invariably produces an ordered B2 matrix decorated by C14 and A15 intermetallic phases, reflecting the strong thermodynamic driving force for chemical segregation and long-range ordering. Our results show that these transformations can be bypassed when the relevant diffusion and ordering processes are outpaced by ultrafast heating and cooling, enabling retention of a metastable disordered A2 solid solution at room temperature.

Two distinct but interconnected kinetic mechanisms underpin this stabilization. Within the molten zone, rapid liquid–solid transformation produces microsegregation on the sub-micrometer scale while suppressing

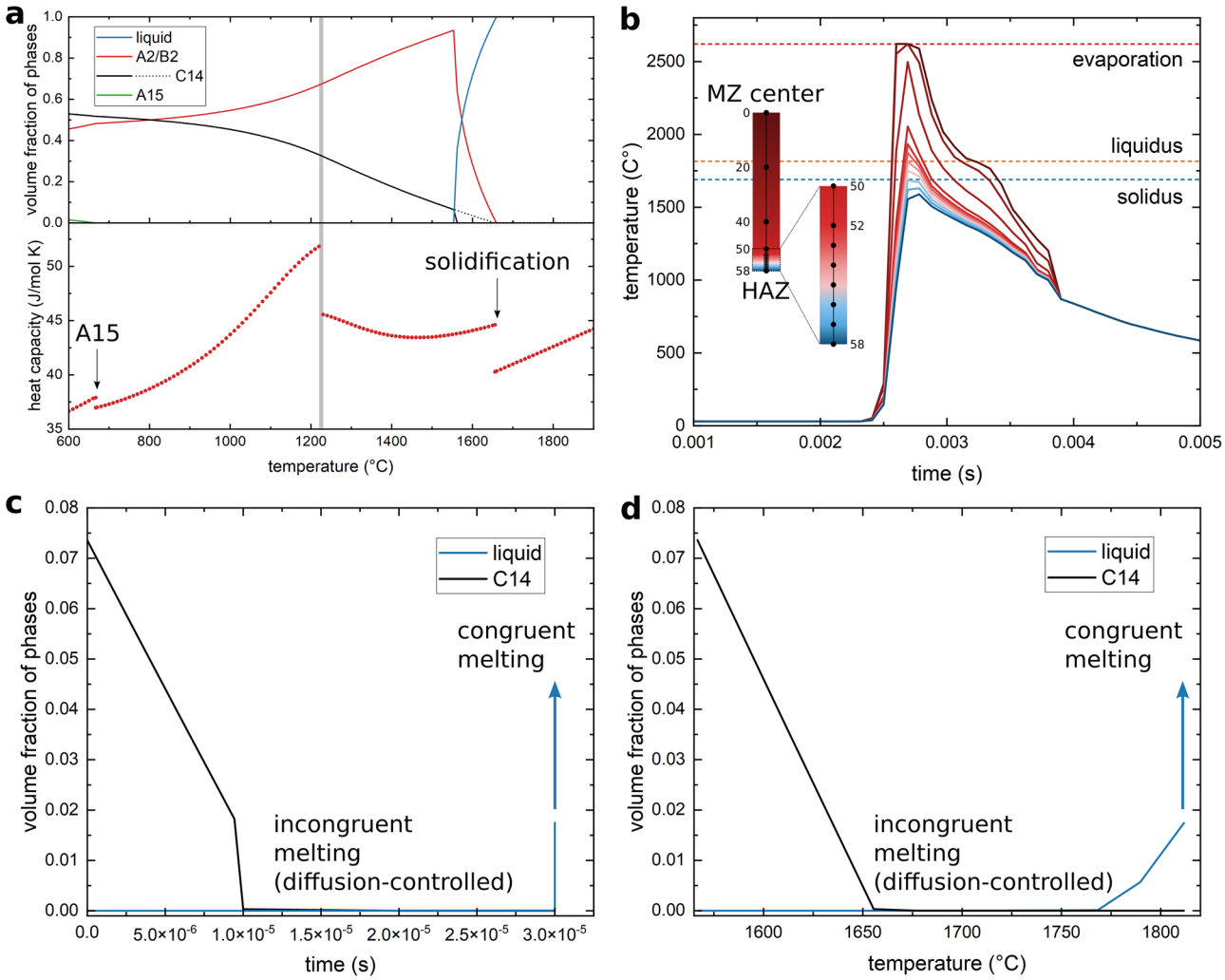

Fig. 3 | Competition between thermodynamic driving forces and kinetic constraints. a Calculated equilibrium phase fractions of NbMoCrTiAl as a function of temperature, indicating stability of the disordered A2 phase only at elevated temperatures and predicted formation of ordered B2 and C14/A15 intermetallic phases upon cooling. The heat-capacity change indicates the A2/B2 transition at 1220–1230 °C (gray area). **b** Simulated transient temperature profile across the melt pool and heat-affected zone, highlighting regions exceeding the B2 disordering temperature and locally approaching the solidus. **c** and **d** Diffusion simulations illustrating dissolution of intermetallic phases during rapid heating and suppression of reprecipitation during subsequent quenching. These results demonstrate that ordering and intermetallic formation are bypassed when transformation timescales are outpaced by heating and cooling rates.

intermetallic nucleation. The high cooling rates prevent the partitioning and long-range diffusion required for C14 and A15 formation. More unexpectedly, in the heat-affected zone, solid-state transformations alone are sufficient to dissolve intermetallic precipitates and disorder the B2 matrix without complete melting. Thermodynamic analysis indicates that B2 becomes unstable above the ordering temperature range of 1220–1230 °C and A15 dissolves at intermediate temperatures (~670 °C), while the Laves phase remains stable up to the solidus. However, finite element and diffusion simulations reveal that the short residence time near the solidus limits the extent of incongruent melting and long-range diffusion, indicating that Laves dissolution can proceed without reprecipitation during subsequent cooling. As a result, ordering and intermetallic formation are kinetically suppressed across a spatial gradient extending beyond the melt pool.

This kinetic suppression fundamentally alters the mechanical response of the alloy. The intrinsically brittle microstructure of high-Al RCCAs arises from two reinforcing mechanisms: restricted dislocation mobility in the ordered B2 matrix and crack initiation at precipitate-decorated grain boundaries. By stabilizing a precipitate-free disordered A2 phase, both constraints are alleviated simultaneously. The reduction in hardness and elastic modulus, together with the pronounced plastic deformation observed in microbending, indicates restored dislocation activity and likely suppression of intergranular fracture. Importantly, this improvement is achieved without modifying alloy composition, thereby preserving the density reduction and oxidation benefits associated with high aluminum content.

More broadly, these findings highlight that kinetic pathway design can extend the accessible phase space of compositionally complex alloys beyond equilibrium predictions, particularly in systems where undesired equilibrium phases are thermodynamically favored but kinetically avoidable under rapid thermal processing. In systems with strong negative mixing enthalpies, ordering and intermetallic formation are often considered unavoidable consequences of composition. Our results demonstrate that these transformations can be kinetically circumvented if processing conditions constrain the relevant diffusion timescales. This suggests that additive manufacturing and other extreme-gradient processes should not be viewed solely as shaping technologies, but as tools for phase-space engineering in multicomponent alloys. This single-track thermal-cycle analysis therefore provides a basis for interpreting the more complex thermal histories that arise from track overlap and repeated reheating in multilayer additive manufacturing.

The ability to selectively stabilize metastable disordered states opens new opportunities for alloy design. Rather than adjusting composition to

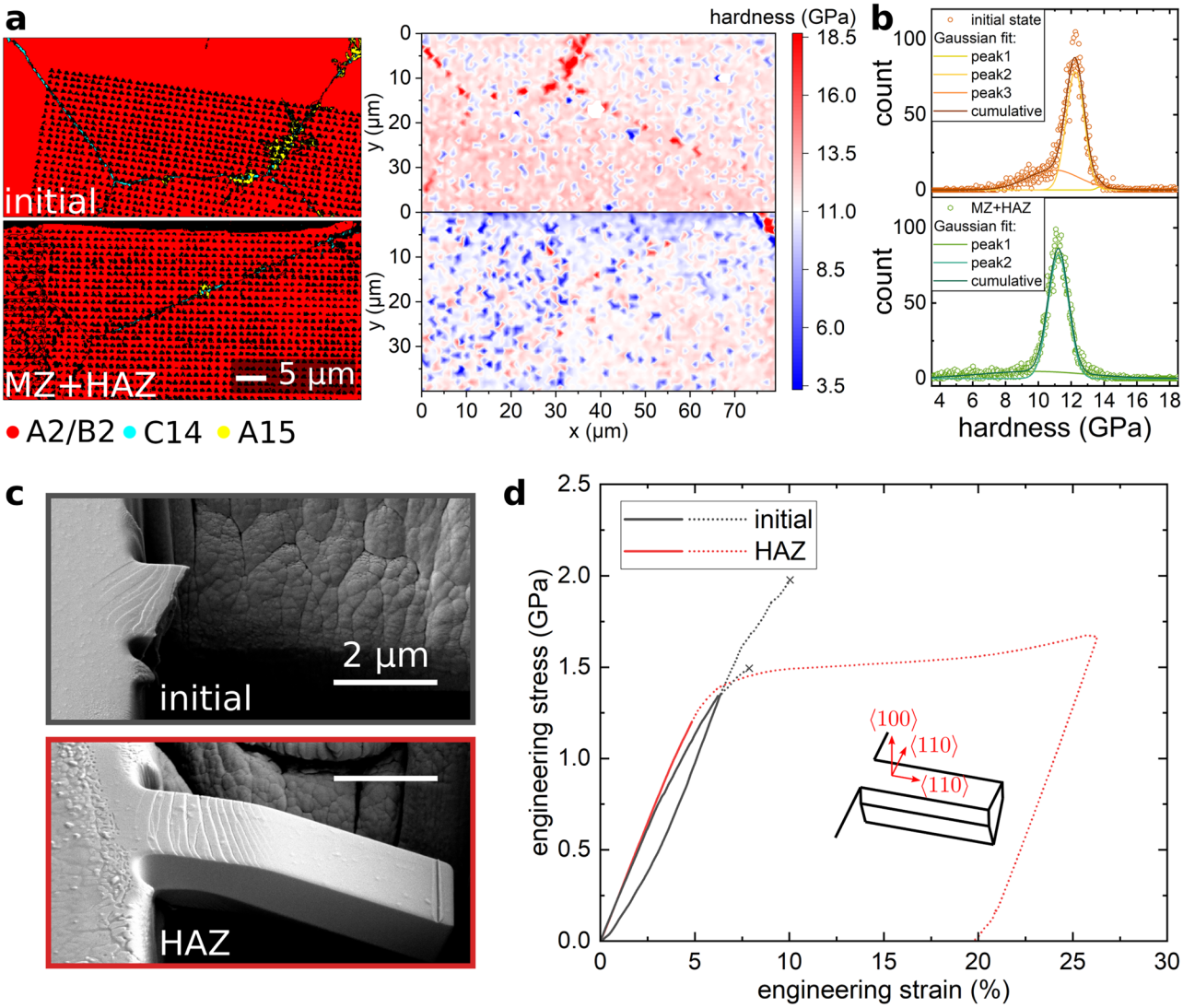

Fig. 4 | Kinetic stabilization of a disordered matrix restores room-temperature plasticity. a Correlative phase and high-resolution nanoindentation hardness maps across the laser-affected region, showing reduced hardness relative to the initial ordered microstructure. **b** Statistical distribution of hardness values before and after processing, illustrating the disappearance of the high-hardness population associated with intermetallic phases. **c** Representative microcantilever bending response of the initial B2-containing microstructure, exhibiting brittle fracture shortly after yielding, and corresponding cantilever fabricated within the A2-stabilized region, showing sustained plastic deformation and dense slip activity near the fixed end. **d** Engineering stress–strain curves of initial B2 and stabilized A2 cantilevers showing brittle fracture in the initial state and significant post-yield bending deformation in the A2-indexed region while exhibiting comparable yield stresses (>1.2 GPa). Solid lines indicate the elastic regime described by simple-beam theory, while dotted lines indicate the post-yield regime discussed in the Supplementary information. The transition from an ordered, precipitate-decorated microstructure to a disordered A2 matrix alleviates both restricted dislocation mobility and grain-boundary crack initiation, enabling enhanced ductility without altering composition.

avoid brittle ordered phases—often at the expense of density, oxidation resistance, or high-temperature strength—kinetic control provides an orthogonal design variable. In NbMoCrTiAl, previous work and the initial microstructure show that its room-temperature brittleness is associated with the ordered B2 matrix and grain-boundary C14/A15 precipitates, while conventional mitigation generally requires reducing the Al content[8,9]. Such an approach may be particularly powerful in refractory systems where sluggish diffusion and high melting temperatures already impose long transformation timescales. Extending this concept to other high-entropy and compositionally complex alloys could enable systematic exploration of kinetically extended phase diagrams, in which mechanical properties are programmed through controlled access to metastable states[22–24].

In this context, non-equilibrium thermal processing refers to rapid local thermal cycling. This thermal cycling enables access to a microstructure away from the equilibrium B2/intermetallic-containing state by kinetically bypassing detectable long-range B2 ordering and intermetallic precipitation. By exploiting the competition between thermodynamic driving forces and kinetic limitations, it becomes possible to decouple composition from microstructural inevitability. The present work illustrates that even in alloys predisposed to ordering and intermetallic formation, ductile, precipitate-free A2-indexed regions can be locally retained through rapid thermal cycling. This expands the design landscape of refractory complex alloys and underscores the broader principle that phase stability in multicomponent systems is fundamentally a function of both composition and time.

In conclusion, we show that extreme thermal gradients can kinetically suppress ordering and intermetallic formation in a high-aluminum refractory compositionally complex alloy, stabilizing a ductile disordered solid solution otherwise inaccessible under equilibrium processing. By constraining diffusion and transformation timescales, non-equilibrium thermal cycling expands the accessible phase space beyond equilibrium predictions. This establishes kinetic control as a design variable in

multicomponent alloys and highlights phase-space engineering as a route to reconcile strength, plasticity, and compositional requirements in high-temperature materials.

Methods

Sample preparation

The fully homogenized equiatomic NbMoCrTiAl sample (~5 × 4 × 2 mm^3, length × width × thickness) was cold-mounted, ground, and gently polished. The final polishing step used an OP-A (acidic alumina) suspension with a grain size of 0.05 μm to achieve a surface quality suitable for microscopic characterization. The composition and processing details of the as-homogenized sample can be found in refs. 1, 25. After microstructural characterization, the mirror-smooth surface was reground using grit P2500 SiC paper to reduce reflectivity and ensure suitability for the laser treatment. After laser treatment, the sample was cold-mounted, then ground and polished to prepare a cross-section for microstructural and mechanical characterization.

Selective laser melting

A series of single-track parallel laser scans was performed using a laser powder bed fusion system (Aconity MIDI+ equipped with a 1 kW nLight laser), targeting a reference melting temperature of 1712 °C, as calculated via CALPHAD[1]. The laser power was varied from 100 to 700 W, while the oxygen level was maintained below 650 ppm throughout. Scanning speed and spot diameter were kept constant at 500 mm s^{-1} and 0.08 mm, respectively, scanning against gas flow direction to avoid interference of any spatter or fumes generated during melting. The line spacing was adjusted according to laser power to prevent overlapping of melt pools and heat-affected zones. Specifically, the inter-track spacing was 0.2 mm for 100–200 W, 0.3 mm for 200–400 W, 0.4 mm for 400–550 W, and 0.5 mm for 550–700 W. A waiting period of at least one minute was maintained after each scan. The cross-sectional overview of melt pools is shown in Fig. S.1 in the Supplementary information.

Microstructural characterization

Electron backscatter diffraction (EBSD, HKL Nordlys and NordlysNano, Oxford Instruments, UK) was performed in a field-emission scanning electron microscope (SEM, Zeiss Merlin, Zeiss, Germany) to obtain phase maps and crystallographic orientation data across the molten and heat-affected regions. Phase identification was supported by energy-dispersive X-ray spectroscopy (EDS, X-Max Extreme, Oxford Instruments, UK). After laser processing, the cross-section was scanned at a step size of 4.46 μm. Regions containing initial grain boundaries and triple points, as well as the molten regions, were scanned with a smaller step size of 0.09 μm. The microstructures were characterized before and after laser processing.

Transmission electron microscopy (TEM) and scanning transmission electron microscopy (STEM) were conducted on focused ion beam (FIB)-prepared lamellae (Helios Nanolab 600i, Thermo Fisher Scientific, formerly FEI, USA) extracted from selected regions. STEM imaging was performed at an acceleration voltage of 300 kV and with a semi-convergence angle of 25.2 mrad in an aberration-corrected Spectra 300 microscope (Thermo Fisher Scientific, formerly FEI, Netherlands) equipped with a high-brightness field-emission electron gun. A semi-collection angle of 69–200 mrad for mass-thickness contrast-related high-angle annular dark-field (HAADF) was used. 4D-STEM and EDS were performed at an acceleration voltage of 100 kV in a Tescan Tensor STEM (Tescan, Brno, Czech Republic), equipped with a symmetrical windowless dual EDS detector.

Atom probe tomography (APT) specimens were prepared by site-specific FIB lift-out from the molten and heat-affected zones (Supplementary information Fig. S.2). Five APT specimens were prepared from a 3 μm × 12 μm × 1 μm slab and mounted on Si coupons. The specimens were prepared and sharpened at 30 kV, followed by a final cleaning step at 2 kV to minimize damage. They were then transferred from the FIB into the APT load lock chamber (10^{-7} Torr) within <5 min to avoid oxidation. APT analyses were performed in laser-assisted mode under ultra-high vacuum (10^{-11} Torr) using a local electrode atom probe (LEAP 5000XR, Cameca Instruments Inc., France). Temperature and pulse rate were 60 K and 125 kHz, respectively. Three-dimensional reconstructions and compositional profiles were evaluated using the commercial software AP Suite.

Mechanical characterization

High-resolution nanoindentation mapping was conducted across grain boundaries and the laser-affected region using an in-situ Nanoindenter (FT-NMT04, FemtoTools, Switzerland) in continuous stiffness measurement mode equipped with a Berkovich tip and operated in an SEM (Supra 50 VP, Zeiss, Germany). An indentation spacing of 1 μm was selected to ensure statistical sampling of microstructural features while minimizing interaction between adjacent indents. The maximum indentation depth was 100 nm. Each array consisted of an 80 × 80 grid of indents. Hardness and elastic modulus were determined by averaging over a depth range of 50–90 nm to ensure a balance between resolution and data quality. Cluster analysis and multi-peak fit analysis of the hardness distributions were conducted to distinguish mechanical populations associated with ordered and disordered regions. A Gaussian mixture model with a Bayesian information criterion[26] was used. Details can be found in the Supplementary information (Fig. S.6).

Microcantilevers were fabricated using a plasma-focused ion beam (P-FIB, Helios 5 PFIB CXe, Thermo Fisher Scientific, USA) from both the initial and laser-processed regions. Cantilevers with a pentagonal cross-section, having a width of ~5 μm and a length of ~15 μm, were oriented to probe grain-boundary and intragranular deformation behavior. Cantilevers with different microstructures were prepared, i.e., A2 and B2 with a defined crystallographic orientation of ⟨110⟩–⟨110⟩–⟨100⟩ along the rolling, transverse, and normal directions, respectively. Bending experiments were conducted by applying a load at the free end of the cantilevers using a 70° wedge-shaped indenter tip with a length of 10 μm in a nanoindenter (sm@rt 500, SURFACE systems + technology, Germany), at a constant loading rate of 0.025 mN/s. The loading direction of cantilevers was along ⟨110⟩. The load–displacement curves were corrected for load frame compliance using indentation data obtained with the wedge-shaped tip on bulk materials near the beams.

Thermodynamic and kinetic simulations

The thermodynamic quantities and phase diagram were calculated using Thermo-Calc software together with the TCHEA7 (High Entropy Alloy v7.0) thermodynamic database. For the representative 150 W condition, the input compositions for the thermodynamic and kinetic simulations were determined from the APT measurement of the corresponding analyzed regions (e.g., chemical concentration in Supplementary Information Fig. S.5). Finite element method (FEM) simulations of the melt pool were performed using the additive manufacturing (AM) module of Thermo-Calc software. The heat source parameters were first calibrated using a steady-state simulation based on experimental melt pool dimensions. A transient simulation was then performed using the calibrated heat source from the steady-state simulation to obtain the time–temperature thermal profiles of the melt pool and its vicinity. The time–temperature profiles were then used to perform Dictra simulations to provide insights into diffusion and the interplay between melting and Laves phase dissolution. DICtra simulations were performed using the homogenization model. A 50 μm planar region consisting of the equilibrium fraction of BCC and Laves phases was first defined in the simulation. The liquid was defined as a second region containing only liquid as a dormant phase, which started to form when the temperature reached the solidus.

Data availability

The data supporting the findings of this study are available in this article, in the supplementary information, and in the data repository at https://doi.org/10.26165/JUELICH-DATA/Z4DHET. Additional data related to this article are available from the corresponding author upon reasonable request.

Received: 31 March 2026; Accepted: 14 August 2026;
Published online: 25 August 2026

References

1. Chen, H. et al. Microstructure and mechanical properties at elevated temperatures of a new Al-containing refractory high-entropy alloy Nb–Mo–Cr–Ti–Al. *J. Alloy. Compd.* **661**, 206–215 (2016).
2. Senkov, O., Woodward, C. & Miracle, D. Microstructure and properties of aluminum-containing refractory high-entropy alloys. *JOM* **66**, 2030–2042 (2014).
3. Senkov, O., Senkova, S. & Woodward, C. Effect of aluminum on the microstructure and properties of two refractory high-entropy alloys. *Acta Mater.* **68**, 214–228 (2014).
4. George, E. P., Raabe, D. & Ritchie, R. O. High-entropy alloys. *Nat. Rev. Mater.* **4**, 515–534 (2019).
5. Müller, F. et al. On the oxidation mechanism of refractory high entropy alloys. *Corros. Sci.* **159**, 108161 (2019).
6. An, Z. et al. Negative mixing enthalpy solid solutions deliver high strength and ductility. *Nature* **625**, 697–702 (2024).
7. Müller, F. et al. Formation of complex intermetallic phases in novel refractory high-entropy alloys NbMoCrTiAl and TaMoCrTiAl: thermodynamic assessment and experimental validation. *J. Alloy. Compd.* **842**, 155726 (2020).
8. Wang, J., Basu, S., Kauffmann, A., Heilmaier, M. & Schwaiger, R. The effect of grain boundaries and precipitates on the mechanical behavior of the refractory compositionally complex alloy NbMoCrTiAl. *Appl. Phys. Lett.* **124**, 201905 (2024).
9. Wang, J., Peter, N. J., Heilmaier, M. & Schwaiger, R. A micromechanical investigation of plasticity in ordered NbMoCrTiAl and disordered TaNbHfZrTi refractory compositionally complex alloys at room temperature. *Int. J. Plast.* **197**, 104593 (2025).
10. Laube, S. et al. Controlling crystallographic ordering in Mo–Cr–Ti–Al high entropy alloys to enhance ductility. *J. Alloy. Compd.* **823**, 153805 (2020).
11. Lu, Y. et al. Additive manufacturing of a functionally graded high entropy alloy using a hybrid powder-bed wire-based direct energy deposition approach. *Addit. Manuf.* **63**, 103424 (2023).
12. Laube, S. et al. Formation and thermal stability of two-phase microstructures in Al-containing refractory compositionally complex alloys. *Sci. Technol. Adv. Mater.* **23**, 692–706 (2022).
13. Laube, S. et al. Strength of disordered and ordered Al-containing refractory high-entropy alloys. *Adv. Eng. Mater.* **26**, 2301797 (2024).
14. Laube, S. et al. Microstructure tailoring of Al-containing compositionally complex alloys by controlling the sequence of precipitation and ordering. *Acta Mater.* **218**, 117217 (2021).
15. Zhang, Y. et al. The microstructure evolution and deformation mechanism of A2/B2 coherent refractory high entropy alloys by low-cost laser in-situ alloying. *J. Alloy. Compd.* **1036**, 181668 (2025).
16. Qi, J. et al. Integrated design of aluminum-enriched high-entropy refractory B2 alloys with synergy of high strength and ductility. *Sci. Adv.* **10**, eadq0083 (2024).
17. Mooraj, S. et al. Crack mitigation in additively manufactured $AlCrFe_2Ni_2$ high-entropy alloys through engineering phase transformation pathway. *Commun. Mater.* **5**, 101 (2024).
18. Zhang, W., Chabok, A., Kooi, B. J. & Pei, Y. Additive manufactured high entropy alloys: a review of the microstructure and properties. *Mater. Des.* **220**, 110875 (2022).
19. Jarlöv, A. et al. Recent progress in high-entropy alloys for laser powder bed fusion: design, processing, microstructure, and performance. *Mater. Sci. Eng.: R: Rep.* **161**, 100834 (2024).
20. Liu, S., Dun, C., Urban, J. J. & Swihart, M. T. Non-equilibrium synthesis methods to create metastable and high-entropy nanomaterials. *Adv. Sci.* **13**, e21953 (2026).
21. Chen, H. et al. Crystallographic ordering in a series of Al-containing refractory high entropy alloys Ta–Nb–Mo–Cr–Ti–Al. *Acta Mater.* **176**, 123–133 (2019).
22. Chang, X., Zeng, M., Liu, K. & Fu, L. Phase engineering of high-entropy alloys. *Adv. Mater.* **32**, 1907226 (2020).
23. Wakai, A. et al. Harnessing metastability for grain size control in multiprincipal element alloys during additive manufacturing. *Nat. Commun.* **16**, 1446 (2025).
24. Gao, S. et al. Additive manufacturing of alloys with programmable microstructure and properties. *Nat. Commun.* **14**, 6752 (2023).
25. Chen, H. *Gefüge und Eigenschaften von äquiatomaren Legierungen aus dem System Ta–Nb–Mo–Cr–Ti–Al*. Ph.D. thesis, Karlsruher Institut für Technologie (KIT) - KIT-Bibliothek <90>; kostenfrei <LFER>, https://doi.org/10.5445/IR/1000118090 (2020).
26. Zhang, C., Bos, C., Sandfeld, S. & Schwaiger, R. Unsupervised learning of nanoindentation data to infer microstructural details of complex materials. *Front. Mater.* **11**, 1440608 (2024).

Acknowledgements

This research was financially supported by the Deutsche Forschungsgemeinschaft (DFG), Grant Nos. SCHW855/6-1 and JA2482/3-2 within the Priority Program SPP2006 “Compositionally Complex Alloys—High Entropy Alloys (CCA-HEA)”. The homogenized NbMoCrTiAl sample was kindly provided by the Group Heilmaier from the Institute for Applied Materials, Karlsruhe Institute of Technology (KIT). The sample preparation and characterization were kindly supported by Mr. Bartsch, Dr. Wessel, and Dr. Grüner from IMD-1. This work contains results obtained from experiments performed at the Ernst Ruska-Centre (ER-C) for Microscopy and Spectroscopy with Electrons at the Forschungszentrum Jülich (FZJ) in Germany. The ER-C beam-time access was provided via the [FZJ_IEK-2_NP1].

Author contributions

J.W.: Conceptualization, data curation, formal analysis, investigation, methodology, visualization, writing—original draft, and writing—review and editing. N.J.P.: Conceptualization, data curation, investigation, visualization, and writing—review and editing. L.H.: Data curation, investigation, visualization, writing—review and editing. A.K.d.S: Formal analysis, investigation, methodology, visualization, writing—review and editing. F.S.: Data curation, investigation, and writing—review and editing. E.A.J.: Investigation, resources, and writing—review and editing. R.S.: Funding acquisition, methodology, project administration, resources, supervision, writing—original draft, and writing—review and editing.

Funding

Open Access funding enabled and organized by Projekt DEAL.

Competing interests

The authors declare no competing interests.

Additional information

Supplementary information The online version contains supplementary material available at https://doi.org/10.1038/s43246-026-01342-3.

Correspondence and requests for materials should be addressed to Jin Wang or Ruth Schwaiger.

Peer review information *Communications Materials* thanks Lanhong Dai, Shanmugasundaram Thangaraju and the other, anonymous, reviewer(s) for their contribution to the peer review of this work. A peer review file is available.

Reprints and permissions information is available at http://www.nature.com/reprints

Publisher’s note Springer Nature remains neutral with regard to jurisdictional claims in published maps and institutional affiliations.

Open Access This article is licensed under a Creative Commons Attribution 4.0 International License, which permits use, sharing, adaptation, distribution and reproduction in any medium or format, as long as you give appropriate credit to the original author(s) and the source, provide a link to the Creative Commons licence, and indicate if changes were made. The images or other third party material in this article are included in the article's Creative Commons licence, unless indicated otherwise in a credit line to the material. If material is not included in the article's Creative Commons licence and your intended use is not permitted by statutory regulation or exceeds the permitted use, you will need to obtain permission directly from the copyright holder. To view a copy of this licence, visit http://creativecommons.org/licenses/by/4.0/.

© The Author(s) 2026